Check for updates

Microstructure and local electrical behavior in [(Nd₂Ti₂O₇)₄/(SrTiO₃)ₙ]₁₀ (n = 4–8) superlattices

Thomas Carlier,[a] Anthony Ferri, [ID][a] Sébastien Saitzek, [ID][a] Marielle Huvé,[a]
Alexandre Bayart,[a] Antonio Da Costa, [ID][a] Rachel Desfeux [ID]*[a] and Antonello Tebano[b]

Artificial [(Nd₂Ti₂O₇)₄/(SrTiO₃)ₙ]₁₀ superlattices (n = 4 and 8) were successfully epitaxially grown on SrTiO₃ substrates by pulsed laser deposition using the *in situ* high energy electron diffraction reflection diagnostic. The crystallographic relationships between Nd₂Ti₂O₇ (NTO) and SrTiO₃ (STO) (layers and substrate) were: $[100]_{NTO}//[001]_{STO}$, $[010]_{NTO}//[\bar{1}10]_{STO}$, and $(00l)_{NTO}//(110)_{STO}$. Nanoscale current variation was detected on both superlattices, with the (NTO₄/STO₄)₁₀ heterostructure showing a higher density. The (NTO₄/STO₄)₁₀ sample did not show a piezoelectric response when measured by piezo-force microscopy (PFM), while ambiguous piezoactivity was observed on the (NTO₄/STO₈)₁₀ superlattice. Scanning transmission electron microscopy energy dispersive spectroscopy analysis showed the diffusion of Nd^{3+} cations on Sr^{2+} sites in SrTiO₃ structure into the multilayers, which was more pronounced when the value of n was lower. These particular nanoscale electrical behaviors, evidenced by electrical conducting channels and misleading PFM signals, were mainly attributed to the presence of oxygen vacancies in the SrTiO₃ layers at higher concentrations near the interface and to the mixed valence state of the titanium (Ti^{3+}/Ti^{4+}). This work showed the strong influence of interface structure on nanoscale electrical phenomena in complex oxide superlattices.

Introduction

With the development of nanotechnology, transition metal oxide thin films with perovskite-type structures have been increasingly investigated in recent years due to their recognized technologically important properties, such as high-temperature superconductivity, colossal magnetoresistance, ferroelectricity and, more recently, multiferroicity.[1] Particular interest has been paid to ferroelectric/piezoelectric lanthanide titanium oxides with a perovskite-layered structure (Ln₂Ti₂O₇ family) due to their high Curie temperatures (T_c, ~1500 °C) which show promise for applications under harsh environments, such as in transducers for motors and aerospace.[2–4] These oxides include La₂Ti₂O₇ (LTO), Ce₂Ti₂O₇, Pr₂Ti₂O₇, and Nd₂Ti₂O₇ (NTO) thin films, in addition to Sm₂Ti₂O₇ and Gd₂Ti₂O₇ thin film-stabilized metastable phases.[5–12] Furthermore, these compounds were lead-free, which is crucial for integrating substances into (nano-)devices because this is now recognized as an important criterion for both the environment and human health.[13] In contrast, these titanates have been shown to possess many other remarkable properties, including high dielectric constants, nonlinear optical activity, photocatalysis, and

photoluminescence.[14–17] Furthermore, LTO in thin films is identified as a highly resistant candidate for ion-beam irradiation.[18] The coexistence of various properties within a unique material seems exciting when many functions are required for applications. The specific NTO oxide explored in this work crystallizes as a single-crystal in a perovskite-layered monoclinic structure with a $P2_1$ space group: $a = 7.68(2)$ Å, $b = 5.48(2)$ Å, $c = 13.02(3)$ Å and $\beta = 98°28'(5)$.[19] It also has a T_c of 1482 ± 5 °C, a spontaneous polarization (P_s) of 9 μC cm⁻², and a coercive field (E_c) of 200 kV cm⁻¹ at room temperature.[4,19] Recently, we successfully grew perovskite-layered ferroelectric NTO thin films through both a sol–gel route and pulsed laser deposition (PLD) on SrTiO₃ (STO) substrates.[8,9,20] Furthermore, the introduction of insulating STO layers within ferroelectric layers to form artificial superlattices has been shown to be promising for modulating the physical properties of thin films.[21–24] For example, improved ferroelectric properties have been reported for BaTiO₃ (BTO)/STO superlattices,[25–27] while for BiFeO₃ (BFO)/STO superlattices, a reduced leakage current was observed in the symmetric superlattices.[28–30]

Herein, we report the growth of (NTO₄/STOₙ)₁₀ (n = 4 and 8) superlattices on STO substrates using PLD combined with conventional reflection high energy electron diffraction (RHEED) system. In particular, the nanoscale electrical behavior and atomic arrangement were investigated to obtain a better understanding of the physical phenomena of these artificial structures. Epitaxial growth of the two superlattices

[a]Univ. Artois, CNRS, Centrale Lille, ENSCL, Univ. Lille, UMR 8181, Unité de Catalyse et Chimie du Solide (UCCS), Faculté des Sciences Jean Perrin, Rue Jean Souvraz, SP18, F-62300 Lens, France. E-mail: rachel.desfeux@univ-artois.fr; Tel: +33 321791771
[b]CNR-SPIN, Department of Civil Engineering and Computer Science Engineering, University of Rome, Tor Vergata, Via del Politecnico, 00133, Rome, Italy

was demonstrated using X-ray diffraction (XRD) measurements and RHEED pattern analysis, and was confirmed by scanning transmission electron microscopy (STEM) imaging. Conductivity variations were locally measured for the superlattices using conductive atomic force microscopy (c-AFM), with a higher leakage current obtained for the $(NTO_4/STO_4)_{10}$ heterostructure. For this $(NTO_4/STO_4)_{10}$ sample, no piezo-signal was obtained by piezoresponse force microscopy (PFM), while apparent piezoactivity was detected on the $(NTO_4/STO_8)_{10}$ superlattice that was not primarily due to a pure ferroelectric phenomenon. Such electrical behaviors were principally attributed to point defects in the atomic structure from the substitution of Sr^{2+} by Nd^{3+} in the STO layers, as evidenced by STEM, and the existence of oxygen vacancies.

Experimental

$(NTO_4/STO_4)_{10}$ and $(NTO_4/STO_8)_{10}$ superlattices (74–96 nm thick) and NTO single layers were grown by PLD on (110)-oriented 1.4 at% Nb-doped STO substrates (crystal, Germany) using a KrF excimer laser (Lambda Physik LPX, 248 nm wavelength, pulse width 25 ns). The base pressure in the chamber was reduced to $\sim 10^{-8}$ mbar. The substrate temperature during deposition was maintained at 600 °C and the deposition atmosphere was a mixture of O_2 with 12% ozone at a fixed pressure of 5×10^{-4} mbar. The laser fluency was adjusted to 5 J cm^{-2} and the repetition rate was between 1 and 3 Hz. After growth, films and superlattices were slowly cooled to room temperature over about 30 min under the deposition atmosphere. RHEED diagnostic was used to control the growth and monitor the surfaces and interface qualities of the NTO films and NTO/STO superlattices *in situ*.

For the NTO target, a highly dense ceramic, 2.54 cm in diameter and 5 mm thick, was prepared using a classical solid-state reaction pathway. Briefly, the NTO oxide was prepared from mixtures of dried oxides Nd_2O_3 and TiO_2 in stoichiometric ratios and heated under air at 1100 °C for 12 h with intermediate grinding. The resulting powder was pressed into a disc and sintered at 1250 °C for 12 h. The XRD pattern confirmed the monoclinic cell characteristics of NTO with $a = 7.6745(4)$ Å, $b = 5.4661(1)$ Å, $c = 13.0048(9)$ Å, and $\beta = 98.4394(7)°$. Further details regarding the synthesis parameters are detailed elsewhere.[9] For the STO target, commercial polycrystalline STO (disk diameter, 2.54 cm; $a_{cubic} = 3.905$ Å) from crystal, Germany was used.

A standard two-axis θ–2θ diffractometer ($\lambda_{Cu-K\alpha 1} = 1.5406$ Å) was used to investigate the structural quality of the films and superlattices. High-angle annular dark-field (HAADF) STEM images and energy dispersive spectroscopy (EDS) mapping were obtained using an FEI TITAN Themis 300 system.

Nanoscale electrical experiments were performed using a commercial AFM microscope (MFP-3D, Asylum Research, USA) under ambient conditions. Ferroelectric properties were probed with a Pt/Ir-coated silicon tip and stiff cantilevers (k, ~ 3 N m^{-1}) in dual AC resonance tracking (DART) PFM mode.[31] Conductivity variations were measured through current mapping and I–V characteristics experiments using the c-AFM

technique (ORCA module for MFP-3D instrument). A Ti/Ir-coated silicon-grounded tip and cantilevers with a stiffness of ~ 2.5 N m^{-1} were used. All ORCA experiments were performed by applying a DC bias voltage of -5 V between the grounded tip and the conductive substrate on the same day without changing the probing tip.

Results

The structural properties of the NTO single layer were first characterized to confirm $(00l)$-epitaxial growth onto the (110)-oriented STO substrate, as previously reported when grown by PLD under standard conditions.[8,9] Fig. 1 shows RHEED patterns observed for the STO substrate before deposition (Fig. 1a) and NTO after deposition (Fig. 1b). When comparing these RHEED patterns, we assumed that the crystallographic relationships between NTO and STO were: $[100]_{NTO}//[001]_{STO}$, $[010]_{NTO}//[\bar{1}10]_{STO}$, and $(00l)_{NTO}//(110)_{STO}$. As shown in Fig. 1c, the RHEED intensity oscillations observed during NTO deposition evidenced high-quality layer-by-layer NTO 2D deposition. Two main distinct features were noted. At the start of deposition, four RHEED intensity oscillations were clearly observed, indicating a period of about 25 laser shots for each oscillation. These first four RHEED intensity oscillations were attributed to deposition of the four-perovskite $NdTiO_3$ unit cells. After those first four RHEED intensity oscillations, the period changed, now corresponding to about 115 laser shots. This second feature was attributed to the periodicity produced by the deposition of $Nd_2Ti_2O_7$ unit cells. Notably, the period in this case was expected to be longer than that corresponding to deposition of the four-perovskite $NdTiO_3$ unit cells. Therefore, from the RHEED intensity oscillations, we estimated a deposition rate value of about 0.1 Å per laser shot for NTO. The θ–2θ XRD pattern recorded after deposition (Fig. 1d) confirmed the $(00l)$-orientation of the film with respect to the (110)-plane of the STO substrate with $d_{00l} = 12.88$ Å, which led to $c = 13.01$ Å, as expected. In contrast, the full width at half maximum (FWHM) measured for the rocking curve recorded on the (004) reflection of NTO was 0.08°. This value was comparable with that obtained for the (110) STO substrate reflection, confirming the very low mosaic spread of the film and the high crystallographic quality of the deposited NTO. Furthermore, the NTO deposition rate estimated by the RHEED intensity oscillations was confirmed by the XRD size effect interference fringes around the (004) peak of an eight-unit-cell thick NTO film deposited on the (110)-oriented STO substrate, as shown in Fig. 1e.

Accounting for the deposition rate of NTO, various $(NTO_4/STO_n)_{10}$ superlattices with different n values were deposited on similar substrates with different STO layer thicknesses. Khestanova *et al.* recently reported the fundamental role of the period in such complex artificial ferroelectric superlattices.[32] The authors demonstrated that full-strain short-period superlattices showed a large polarization, which was not the case for longer multilayer periods, indicating that electrostatic boundary conditions were the main factor leading to the ferroelectric response at the expense of strain effects. From these results, our strategy was to fabricate superlattices with
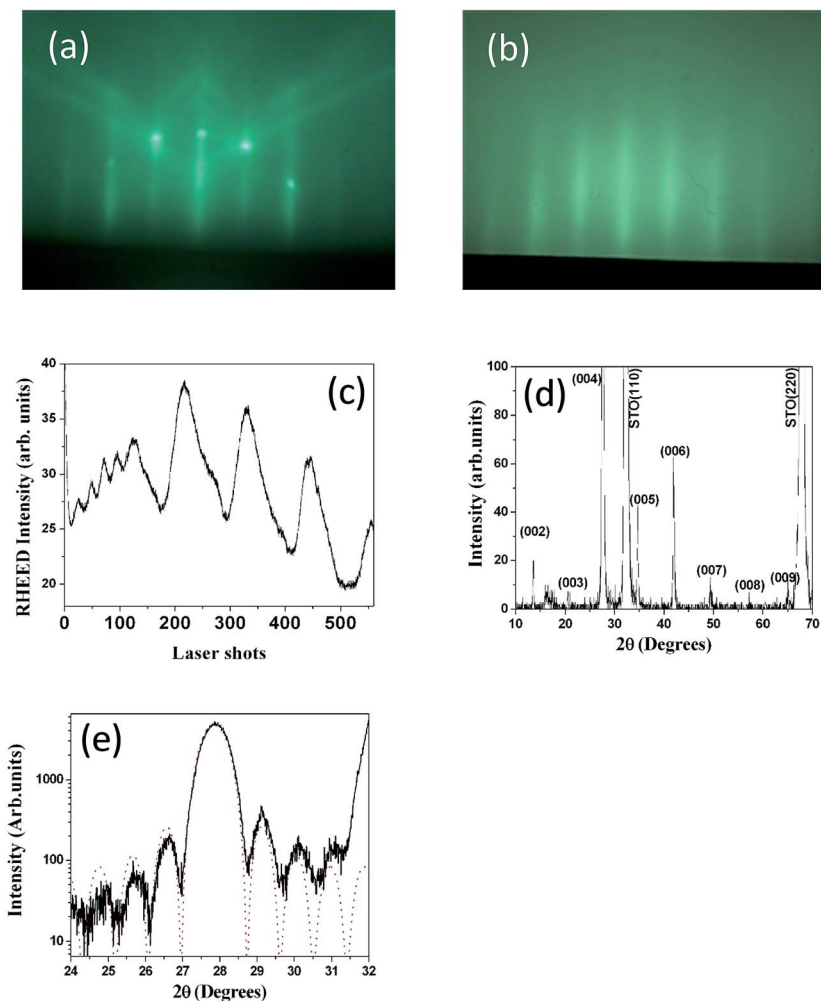
Fig. 1 (a) SrTiO₃ (STO) substrate RHEED pattern; (b) RHEED pattern observed after Nd₂Ti₂O₇ (NTO) deposition; (c) RHEED intensity oscillations observed during NTO deposition; (d) $\theta-2\theta$ XRD pattern of NTO film deposited onto (110)-oriented STO substrate; (e) XRD size effect interference fringes around the (004) peak of an eight-unit-cell-thick NTO film deposited on (110)-oriented STO substrate (dashed line corresponds to experimental data; dotted line corresponds to calculated data).

small n values, namely $(NTO_4/STO_4)_{10}$ and $(NTO_4/STO_8)_{10}$ (74 and 96 nm-thick, respectively). The XRD pattern obtained for the $(NTO_4/STO_4)_{10}$ superlattice is shown in Fig. 2a. As expected, satellites peaks were observed around the two main peaks. The angular distance between the satellite peaks SL_{-1} and SL_{+1} around the SL_0 for the (004) peak provided precise information on the film structure, allowing the lattice parameters of the superlattice unit cell to be evaluated. Through calculations accounting for the angular position of the satellite peaks, we confirmed the 4×4 periodicity of the synthesized $(NTO_4/STO_4)_{10}$ superlattice. Similar results were obtained for the $(NTO_4/STO_8)_{10}$ superlattice. Furthermore, the high quality of the diffraction peaks of these superlattices supported the epitaxial growth of these heterostructures.

During deposition of the $(NTO_4/STO_n)_{10}$ superlattices, RHEED intensity oscillations were not observed. However the streaky RHEED patterns shown in Fig. 2b and c, and those recorded at the end of the deposition of both the NTO and STO layers, preserved the typical features of a quasi-2D deposition

for each layer. Consequently, by considering the RHEED and XRD patterns, we found that good quality epitaxial NTO single layers of $(NTO_4/STO_4)_{10}$ and $(NTO_4/STO_8)_{10}$ superlattices were grown.

In a second step, characterization of the electrical properties of the two fabricated superlattices was conducted. Firstly, PFM experiments to determine the piezo/ferroelectric properties were performed on the $(NTO_4/STO_8)_{10}$ superlattice, consisting of poling and switching experiments. Fig. 3a and b show the AFM morphology and corresponding out-of-plane PFM phase image, where two 'artificial' square-shaped domains of 'upward' (bright contrast, $5 \times 5 \ \mu m^2$) and 'downward' (dark contrast, $2 \times 2 \ \mu m^2$) polarization were locally written by applying DC voltages of -7 V and $+7$ V to the tip, respectively. Polarization switching seemed to be successful, as evidenced by both the well-defined squares and the uniform contrasts obtained after poling experiments, suggesting full switching of domains to one of the two c-oriented polarization states. Furthermore, no surface modification was observed on the corresponding topographic
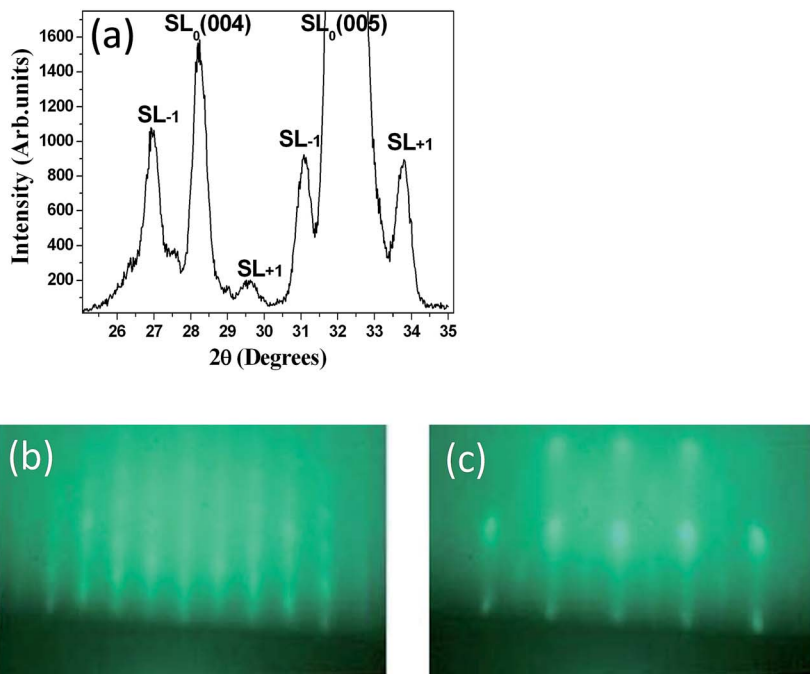
Fig. 2 (a) XRD pattern obtained for $(NTO_4/STO_4)_{10}$ superlattice. RHEED patterns recorded at (b) the end of deposition of the last NTO layer and (c) the last STO layer, for an $(NTO)_4/(STO_8)_{10}$ superlattice.

image, excluding surface electrochemical processes during poling experiments. To further address the switching behavior of ferroelectric domains, remnant piezoresponse loops on the superlattice were measured, as shown in Fig. 3c and d. The phase loop and butterfly-shape of the amplitude loop showed clear hysteretic behavior, suggesting the signature of local ferroelectricity in the superlattice, which was supported by applying the off-field recording method of the piezoloops to minimize the electrostatic effect.[33]

However, considering the complex nature of the physico-chemical phenomena that can exist in such artificial super-lattices (these ones include interlayer diffusion, oxygen vacancies, strains, discrete random and continuous layer thickness fluctuations at the interface)[34] and in order to get a deeper insight on the ferroelectric-like behavior obtained, further PFM experiments were performed. In particular, PFM voltage spectroscopy measurements under different AC driving and maximum DC voltages were conducted. Fig. 3e shows the remnant in-phase piezoloops as a function of the driving voltage. As observed, the loops are insensitive when varying the magnitude of the V_{AC} probing voltage, especially when the V_{AC} was higher than the apparent coercive voltage (about 6 V). This specific behavior was a signature of a non-ferroelectric contri-bution to the observed PFM signal.[35–38] From Fig. 3f, we noted a strong dependence of the remnant loops on the maximum DC voltage applied. Indeed, the opening of the loops continuously increased with increasing DC bias voltage, even once the apparent coercive voltage was reached. Again, this particular behavior cannot be only related to ferroelectric polarization.[39] Consequently, these bias-dependent hysteresis measurements were unable to fully determine that the obtained PFM signals

(poling and loops) were mainly due to the piezo/ferroelectric nature of the $(NTO_4/STO_8)_{10}$ superlattice. Recently, much attention has been paid to such 'false' electromechanical PFM signals, which can be the signature of several phenomena, such as Joule heating, electrostriction, chemical dipoles, charge injection, field effects, Vegard strain, deposition, subsurface damage, surface damage, and vacancy ordering.[36–42] Our results showed that the AFM-tip induced large voltages during PFM analysis, which could explain the hysteretic responses and opposite stable contrasts obtained on the $(NTO_4/STO_8)_{10}$ structure by considering the existence of oxygen vacancies. Furthermore, as already demonstrated, a bistable distribution of such vacancies under electrical bias is responsible for the ferroelectric-like behavior in PFM imaging.[40,43] Additionally, both the loop independence on the probing AC voltage with respect to the apparent coercive voltages and the area increase of the loops with increasing applied maximum voltage were related to an increase in the degree of ionic motion.[38,44] Consequently, we considered ionic conduction and/or the motion of oxygen vacancies to be the main factors responsible for the poling contrasts and hysteretic responses obtained.

Similar PFM tests were undertaken on the $(NTO_4/STO_4)_{10}$ superlattice, but no piezo-signal was obtained, regardless of the imaging method or spectroscopic mode of the DART PFM technique. This result was not expected considering that this short-period superlattice should have better ferroelectric prop-erties, as shown by Khestanova et al.[32]

At this point, c-AFM technique was used to locally probe the eventual leakage currents over the surface of the artificial superlattices. In particular, a leaky behavior could explain the absence of piezoactivity in the $(NTO_4/STO_4)_{10}$ superlattice, and
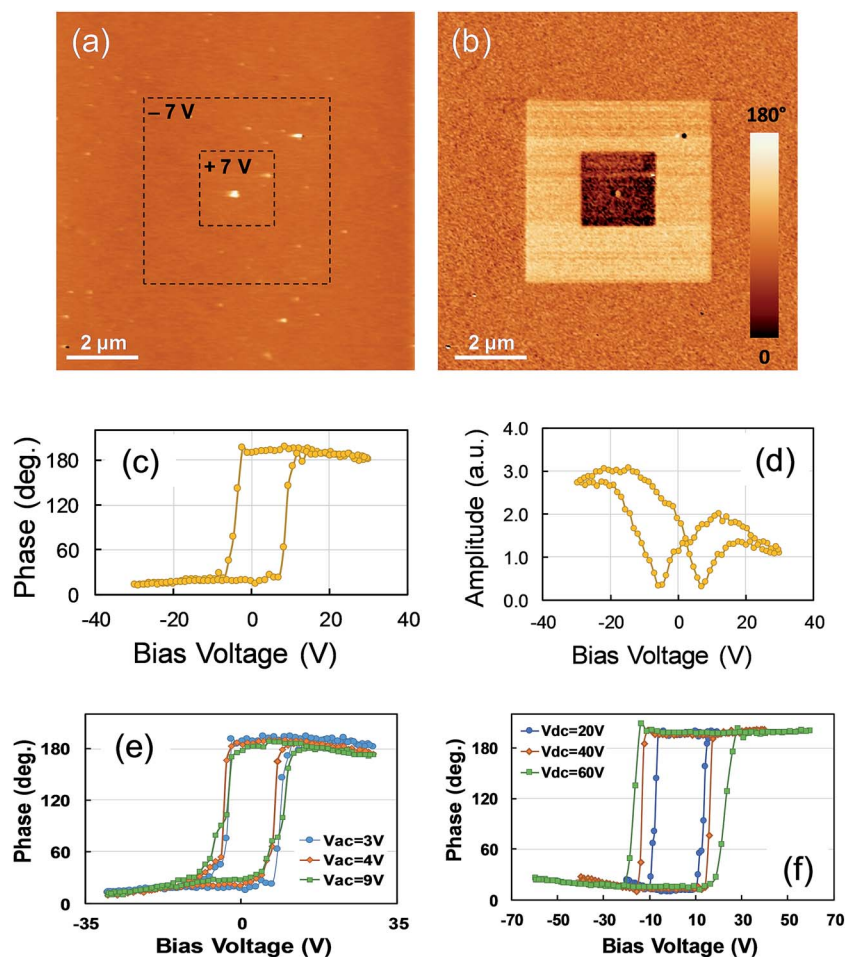
Fig. 3 PFM experiments on the $(NTO_4/STO_8)_{10}$ superlattice. (a) AFM topography and (b) out-of-plane phase PFM images recorded simultaneously. In the PFM images, one square region of 5×5 μm^2 was poled (bright area), then a smaller square region of 2×2 μm^2 was reverse poled (black area) by applying -7 V and $+7$ V, respectively. The scan area is 10×10 μm^2 for both images. Remnant (c) in-phase and (d) in-amplitude piezoresponse loops. (e) In-phase piezoloops under different AC driving voltage and (f) in-amplitude piezoloops for different maximum DC voltage.

also help explain the ambiguous PFM responses observed on the $(NTO_4/STO_8)_{10}$ superlattice. Furthermore, considering our assumption regarding the existing oxygen vacancies, such charged defects could lead to electrical conducting paths detectable by c-AFM. The current distribution was measured by applying a constant DC bias of -5 V between the grounded tip and the conductive substrate. The conductive Ti/Ir-coated AFM tip was used as a movable top electrode. Fig. 4b and d show current mapping with simultaneously recorded topography for the $(NTO_4/STO_8)_{10}$ and $(NTO_4/STO_4)_{10}$ superlattices, respectively. Variations in local conductivity were observed over the scanned regions, as evidenced by the red regions ('hot spots') in the blue background, where a higher conductivity of about -20 pA was detected. The distributions of the leakage current over the heterostructure surface were inhomogeneous, with no obvious correlation existing between the topography and the current image. This contrasted with results from other ferroelectric oxides, wherein both grains and grains boundaries represented a preferential electrical conducting channel.[45–49] For positive bias, no local conductivity could be measured until

+10 V, showing strong asymmetric leakage current characteristics. Local I–V curves were also recorded over the free film surface of the $(NTO_4/STO_8)_{10}$ superlattice by sweeping a DC bias voltage, ranging from -8 and $+8$ V, between the conductive AFM tip and the heterostructure. The I–V characteristics presented in Fig. 4g show a diode-like behavior with a strong asymmetry in conduction behavior according to positive or negative voltages, which was consistent with the current map observed. Furthermore, no current was measured at a positive voltage, while significant conductivity was detected from a bias of around -4.5 V. From these results, a clear difference in detected current was observed between both superlattices, this was because the lateral density of the $(NTO_4/STO_4)_{10}$ heterostructure significantly increased, despite the size of the 'hot spots' not changing, as shown in Fig. 4d. This improvement in the local conductivity could cause the PFM signal to be absent, and could be reasonably attributed to the smallest thickness of the STO slab (4 STO layers). However, as already mentioned, this contradicted with the recent work of Khestanova et al. on BTO/STO superlattices.[32] To verify this assumption, the NTO single layer
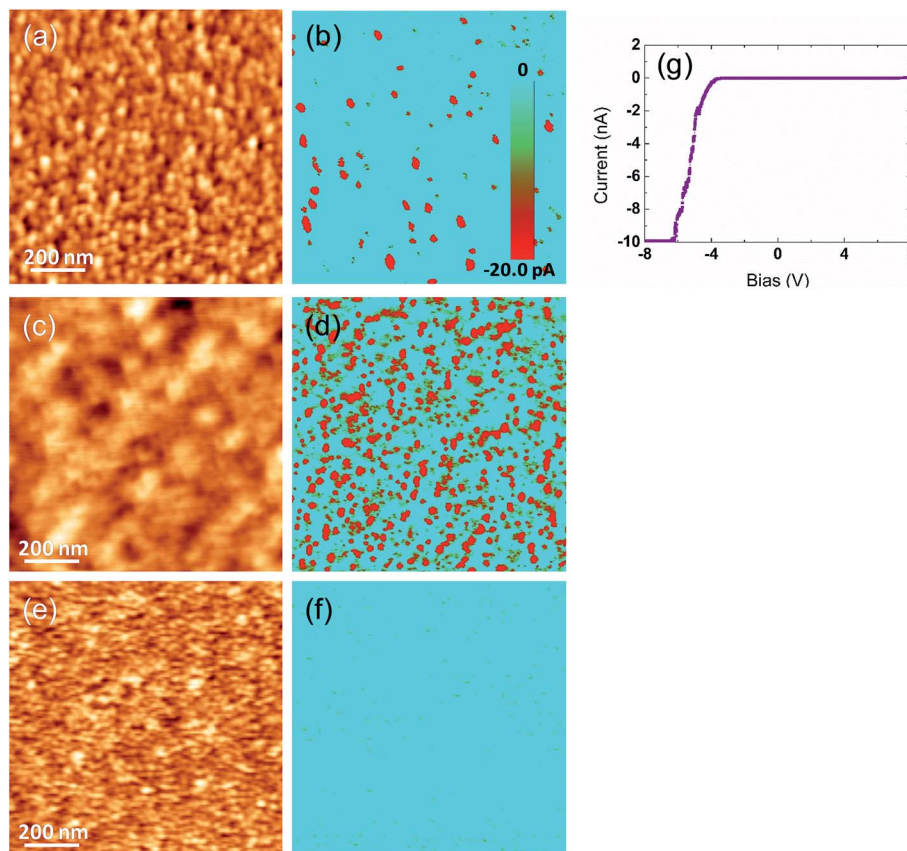
Fig. 4 Local conductivity variations measured by c-AFM. Current mapping under −5 V DC bias measured over the surface of (b) the $(NTO_4/STO_8)_{10}$ superlattice, (d) the $(NTO_4/STO_4)_{10}$ superlattice, and (f) the NTO single layer. Red contrasts show higher local conductivity. Scale bar for the current is similar for all three images. AFM morphologies simultaneously recorded are shown in (a), (c), and (e). Scan area is $1 \times 1\ \mu m^2$. (g) Local I−V characteristics of the $(NTO_4/STO_8)_{10}$ superlattice. At a bias voltage of −6.5 V, the detected current was higher than the detection limit.

was also characterized by c-AFM under similar experimental conditions, and the obtained current map is shown on Fig. 4f. In this case, the detected current was found to be insignificant, as evidenced by the uniform blue contrast in the conduction pattern, which confirmed the insulator nature of the NTO film.

Therefore, the red contrasts observed on Fig. 4b and d suggested that the current passed through all STO layers, allowing for tunneling.[50] To explain the drastic increase in conductivity when the number of STO layers was reduced to four in each slab of the superlattice, three main scenarios are proposed. The first was related to the existence of oxygen vacancies in the STO layers.[51] In the case of LaNiO$_{3−\delta}$ (LNO) ultrathin films grown on STO substrate, Scherwitzl *et al.* hypothesized that the oxygen vacancy concentration might be larger near the interface LNO/STO.[52] This would increase the relative fraction of non-stoichiometric material when the thickness of the film was smaller, explaining the observed metal-insulator transition when the film thickness was decreased.[52] For our NTO/STO superlattices, we also believed the concentration of oxygen vacancies near the NTO/STO interface to be higher than that in the core of the STO layer. This should mean that the relative fraction of nonstoichiometric STO material, which contains mixed valence states of titanium (Ti^{3+}/Ti^{4+}), is higher in the $(NTO_4/STO_4)_{10}$ superlattice than in the $(NTO_4/STO_8)_{10}$

superlattice. Therefore, this phenomenon could favor conductivity in the $(NTO_4/STO_4)_{10}$ superlattice, leading to an increase in electrical conducting channels, as observed in Fig. 4d. Furthermore, as mentioned above, such oxygen vacancies could explain the ambiguous PFM signals obtained for the $(NTO_4/STO_8)_{10}$ structure. In the second scenario, the higher conductivity in $(NTO_4/STO_4)_{10}$ superlattice compared with the $(NTO_4/STO_8)_{10}$ superlattice can be explained by electronic miniband formation in such artificial structures. In their study on the theory of conductivity in superlattice minibands, Yang and Sarma showed that the mobility decreased when the period of the superlattice was increased.[53] In our $(NTO_4/STO_n)_{10}$ system, we have shown that the conductivity increased when n decreased. This result was in good agreement with the theoretical study[53] and could explain the higher conductivity in the $(NTO_4/STO_4)_{10}$ superlattice owing to a higher tunneling probability in this superlattice compared with the $(NTO_4/STO_8)_{10}$ superlattice (whose periodicity was higher). However, the periods of our $(NTO_4/STO_4)_{10}$ and $(NTO_4/STO_8)_{10}$ as-grown superlattices were 74 Å and 96 Å, respectively which were larger than the 40–60 Å range for superlattice periods in the work of Yang and Sarma.[53] Furthermore, as reported by the authors, the miniband width fell exponentially with increasing superlattice period. In contrast, considering that the thickness

of the NTO barrier in both of our superlattices did not change, the increase in the number of STO layers from 4 to 8 should not decrease the conductivity as significantly, as shown in Fig. 4b and d.[54] Therefore, we concluded that this second scenario was not the major cause of conductivity in our superlattices. The third scenario that might explain the higher conductivity in the $(NTO_4/STO_4)_{10}$ superlattice is based on polar discontinuity existing across the NTO/STO heterointerfaces.[55] As reported by Herranz *et al.* in the ideal ionic limit, the $SrTiO_3$ perovskite structure stacks according to the sequence $[O_2]^{4-}/[SrTiO]^{4+}$ along the [110] direction, which is along the growth direction of the NTO film.[56] For the NTO film, along the [001] growth direction, the complex sequence was $[O_2]^{4-}/[NdTiO]^{5+}/[O_2]^{4-}/[TiO]^{2+}/[Nd_2O_4]^{2-}/[TiO]^{2+}/[O_2]^{4-}/[NdTiO]^{5+}$.[17,57] As a result, we assumed that the interfaces between STO and NTO should exhibit polar discontinuity. Furthermore, as reported by Ohtomo *et al.*,[55] polarity discontinuities often arise in naturally layered oxide structures, such as ferroelectric titanates, including layered-perovskite phases constructed as $A_nB_nO_{3n+2}$ for $n = 2$–6, and then the concerned $Nd_2Ti_2O_7$ oxide corresponding to $n = 4$. However, considering that the number of STO/NTO interfaces was the same in the two $(NTO_4/STO_4)_{10}$ and $(NTO_4/STO_8)_{10}$ superlattices, we excluded this scenario to explain different maps measured on the superlattices. Consequently, we concluded that a more plausible scenario explaining the higher conductivity in the $(NTO_4/STO_4)_{10}$ was related to the oxygen vacancies. Furthermore, cation interdiffusion/intermixing at heterointerfaces (Sr^{2+}/Nd^{3+} in our superlattices)

and epitaxial strain in the interfacial layers (STO/NTO in our heterostructures) and octahedral rotations (TiO_6 in our case) through spatial gradient in the electronic structure are known to influence conduction.[56,58–60]

At this stage, greater insight into the atomic structure and interface sharpness of the superlattices was required to explain the local electrical behavior observed above and validate the selected hypothesis. Therefore, we conducted a microstructural study using STEM on the cross-section prepared with a focused ion beam (FIB). Fig. 5 shows a HAADF-STEM image of the $(NTO_4/STO_4)_{10}$ superlattice recorded along the [100] direction. The brightness of the dots on the image was proportional to Z^n, where Z is the average atomic number of the atomic column. The column of Nd^{3+} ions appeared very bright ($Z_{Nd} = 60$), while the Ti^{4+} positions were seen as weak spots ($Z_{Ti} = 22$). As expected, perfect stacking of 4 NTO unit cells and 4 STO unit cells corresponding to 52.0 Å for NTO ($4 \times c_{NTO}$) and 22.1 Å for STO ($4 \times a_{STO}\sqrt{2}$) was observed (Fig. 5a). In the first three layers of NTO, the projection of the [100] structure was perfectly superimposed, except at the level of the blue arrow, where a local defect was detected (Fig. 5b). In the fourth and subsequent NTO layers, this local defect was generalized and periodically repeated, leading to a new structure (Fig. 5c). This could probably be attributed to the gamma phase often detected in NTO thin films and considered a polymorph of NTO.[61] Structural characterization of this phase has yet to be established and will be explored in future work with the help of HAADF-STEM images, electronic precession crystallography, and electron
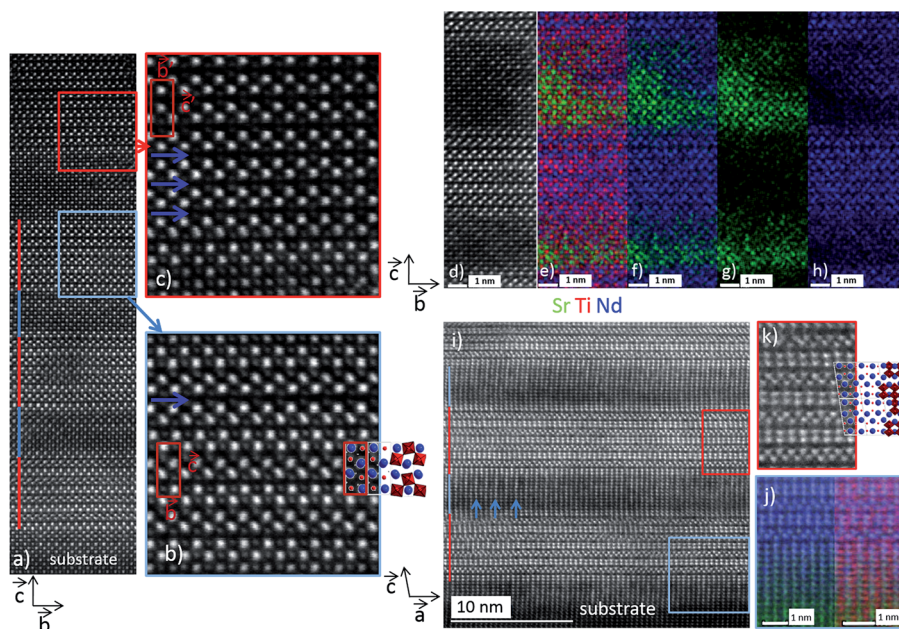

Fig. 5 STEM-EDS analysis of the $(NTO_4/STO_4)_{10}$ superlattice. (a) [100] HAADF image of the first four NTO layers. A regular stacking of 52.0 Å of NTO (red lines) and 22.1 Å (blue lines) of STO is observed. (b) Enlargement of the blue area in the third NTO layer showing a perfect stacking of the NTO, except at the level of the blue arrow, where a local defect is observed. (c) Enlargement of the red area in the fourth NTO layer where the previously defect is periodically repeated, leading to a new structure. (d) [100] HAADF image of the third NTO layer surrounded by two STO layers. EDS mapping of: (e) Sr (green) + Ti (red) + Nd (blue), (f) Sr (green) + Nd (blue), (g) Sr (green), and (h) Nd (blue). Significant Nd diffusion, which replaces Sr in the STO layers, is observed in this area. (i) [010] HAADF image of the first three layers. Red and blue lines indicate NTO and STO layers, respectively. Blue arrows show white lines in the STO layers, which were attributed according to (j) EDS cartography [Sr (green); Nd (blue); Ti (red)] of the substitution of Sr by Nd. (k) Enlargement of the red area showing the perfect [010] projection of the NTO structure.

energy loss spectroscopy (EELS) studies. The diffusion of Nd into the STO layers was considerable, as shown by EDS mapping in the region of the third NTO layer (Fig. 5d–h). The substitution of Sr with Nd in the $SrTiO_3$ structure was not surprising considering the ionic radii of each cation. The ionic radius of Sr^{2+} in the 12-fold coordinated sites was 1.44 Å, and 1.24 Å when the coordination number was eight. In contrast, in the $Nd_2Ti_2O_7$ structure, Nd^{3+} had ionic radii of 1.11 Å and 1.27 Å for 8-fold and 12-fold coordinated sites, respectively.[62] These values were similar, explaining the large diffusion of Nd^{3+} cations observed on the Sr^{2+} sites in the STO structure. Projection of the $[010]_{NTO}$ structure confirmed the previous results (Fig. 5i–k). Ordering the substitution of Sr by Nd was sometimes observed (blue arrows in Fig. 5i). Concerning the $(NTO_4/STO_8)_{10}$ superlattice, the STEM HAADF images of the cross-section performed in the [010] direction of the first two NTO layers (Fig. 6a) also confirmed the stacking of four layers of NTO and eight layers of STO. As for $(NTO_4/STO_4)_{10}$, the same new structure (as described in Fig. 5) appeared after the third NTO layer. EDS mapping (Fig. 6b) also showed the diffusion of Nd into the STO layers. However, this seemed less important than for the $(NTO_4/STO_4)_{10}$ superlattice, with conservation of the structural integrity of $Nd_2Ti_2O_7$ and $SrTiO_3$ between these diffusion zones. To check the intensity of Nd diffusion at the level of STO layers,

Fig. 7 Comparison of the EDS composition of the first three NTO and STO layers in the $(NTO_4/STO_4)_{10}$ and $(NTO_4/STO_8)_{10}$ superlattices. Nd diffusion in the STO layer is greater in the $(NTO_4/STO_4)_{10}$ superlattice. Low Sr diffusion is observed in the NTO layer of the $(NTO_4/STO_8)_{10}$ superlattice.
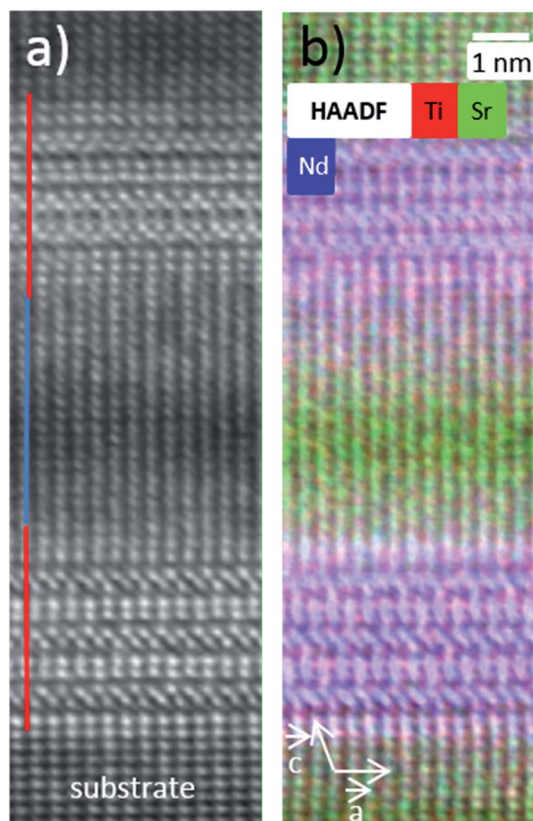

Fig. 6 STEM-EDS analysis on the $(NTO_4/STO_8)_{10}$ superlattice. (a) [010] HAADF image of the first two NTO layers. A regular stacking of 52.0 Å of NTO (red lines) and 44.2 Å of STO (blue lines) is observed. (b) EDS mapping showing a large diffusion of the Nd at the level of the STO layer [Sr (green); Nd (blue); Ti (red)].
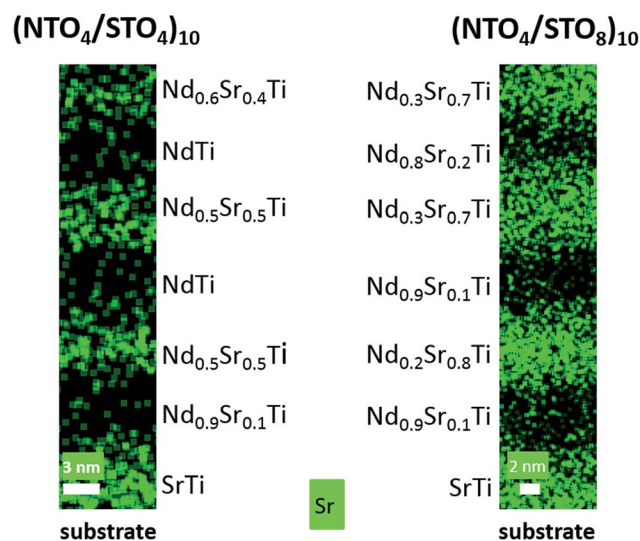
EDS compositions were estimated (Fig. 7). Nd was clearly more present in the STO layer of the $(NTO_4/STO_4)_{10}$ superlattice. The ratio of Nd/Sr was higher in the STO layers of the $(NTO_4/STO_4)_{10}$ superlattice than in the STO layers of the $(NTO_4/STO_8)_{10}$ superlattice, which suggested that the diffusion and compositions were very different towards the boundary. In other words, Nd diffusion was more pronounced near the STO/NTO interfaces within the superlattices, as observed in Fig. 5f and 6b. From these results, we can directly link the local leakage currents observed by c-AFM to the diffusion phenomena for each superlattice. In particular, the higher cationic diffusion found for the thinner STO slab led to higher local conductivity, as observed in the current mapping (Fig. 4). This substitution of Sr^{2+} by Nd^{3+} in the $SrTiO_3$ layer led to the mixed valence state of titanium (Ti^{3+}/Ti^{4+}), as evidenced by Joseph et al.[63] Furthermore, when diffusion was stronger, in the case of the $(NTO_4/STO_4)_{10}$ superlattice, the Ti^{3+}/Ti^{4+} ratio increased and induced modification of the oxygen vacancies to preserve electroneutrality. Therefore, the higher Ti^{3+} content in the STO layers, combined with oxygen vacancies in the STO layers, would lead to higher conductivity in the $(NTO_4/STO_4)_{10}$ superlattice. Furthermore, different mechanisms are known to explain the conductivity/leakage behavior in dielectric thin films and superlattices.[28–30,64–66] Recently, Lu et al. showed the existence of highly conductive channels, 'hot spots', in ferroelectric $SrTiO_3$ thin films emerging due to resonant tunneling through localized electronic states created by polar Ti_{Sr} antisite defects. The authors demonstrated that the defect-assisted tunneling mechanism, where conduction was dominated by 'hopping' through a defect state, played a decisive role in the local electrical properties of thin film $SrTiO_3$ samples.[67] Such conducting paths are very similar to those observed in our study, with identical behavior as a function of the STO thickness, which

allowed the tunneling conduction mechanism to also explain the local conductivity found in our heterostructures. To carefully identify the conductivity mechanism existing in our superlattices, *I–V* curves and further AFM experiments will be considered in future work. Finally, the higher level of Nd diffusion associated with the larger electrical conductivity density might explain the absence of PFM signal in the $(NTO_4/STO_4)_{10}$ superlattice, while lower diffusion corresponding to lower leakage current does not prevent the PFM signals being recorded, but was not mainly attributed to the ferroelectric phenomenon. Furthermore, this result was supported by the probable existence of oxygen vacancies and their migration beneath the probing AFM tip during bias application.

Conclusion

Using a PLD technique with conventional RHEED, epitaxial NTO single layers and $(NTO_4/STO_n)_{10}$ ($n = 4$ and 8) superlattices were grown on Nb-doped (110)-STO substrates. No piezoelectric signal was observed by PFM on the $(NTO_4/STO_4)_{10}$ heterostructure, while ambiguous responses were measured on the $(NTO_4/STO_8)_{10}$ heterostructure. The latter were typical of oxygen vacancy motion and/or ionic species migration under high electrical voltage. Electrical hot spots were locally detected on the surface of both superlattices, with a higher density when n was reduced to 4. EDS mapping showed Nd^{3+} diffusion in the STO layers, with a more pronounced effect observed for the $(NTO_4/STO_4)_{10}$ superlattice. The existence of electrical conducting channels at the nanoscale in the superlattices was attributed to the presence of oxygen vacancies near the NTO/STO interfaces, along with the relative fraction of non-stoichiometric STO material, which increased when the thickness of each STO layer in the superlattice decreased. This high local current density prevented the measurement of PFM signals for the $(NTO_4/STO_4)_{10}$ superlattice, while the PFM activity obtained for the $(NTO_4/STO_8)_{10}$ superlattice could not be attributed to pure ferroelectric polarization behavior, as shown by bias-dependent hysteresis measurements. This study shows that precautions must be taken to carefully interpret local electromechanical signals obtained from classical imaging and spectroscopic modes of contact-resonance PFM. Furthermore, the interfacial structure properties were shown to be crucial for correctly elucidating the nanoscale electrical behavior in such artificial oxide superlattices.

Conflicts of interest

The authors have no conflicts of interest to declare.

Acknowledgements

References

1 S.-W. Cheong, *Nat. Mater.*, 2007, **6**, 927–928.
2 A. Sayir, S. C. Farmer and F. Dynys, *Advances in Electronic and Electrochemical Ceramics*, John Wiley & Sons, 2006, pp. 57–68.
3 J. K. Yamamoto and A. S. Bhalla, *J. Appl. Phys.*, 1991, **70**, 4469–4471.
4 H. Yan, H. Ning, Y. Kan, P. Wang and M. J. Reece, *J. Am. Ceram. Soc.*, 2009, **92**, 2270–2275.
5 J. Fomperyrine, J. W. Seo and J. P. Locquet, *J. Eur. Ceram. Soc.*, 1999, **19**, 1493–1496.
6 Z. Shao, S. Saitzek, P. Roussel, A. Ferri, E. Bruyer, A. Sayede, M. Rguiti, O. Mentre and R. Desfeux, *Adv. Eng. Mater.*, 2011, **13**(10), 961–969.
7 A. Bayart, Z. Shao, A. Ferri, P. Roussel, R. Desfeux and S. Saitzek, *RSC Adv.*, 2016, **6**, 32994–33002.
8 A. Bayart, S. Saitzek, A. Ferri, R. Pouhet, M.-H. Chambrier, P. Roussel and R. Desfeux, *Thin Solid Films*, 2014, **553**, 71–75.
9 A. Bayart, S. Saitzek, M.-H. Chambrier, Z. Shao, A. Ferri, M. Huvé, R. Pouhet, A. Tebano, P. Roussel and R. Desfeux, *CrystEngComm*, 2013, **15**, 4341–4350.
10 S. Havelia, S. Wang, K. R. Balasubramaniam and P. A. Salvador, *J. Solid State Chem.*, 2009, **182**, 1603–1610.
11 Z. Shao, S. Saitzek, A. Ferri, M. Rguiti, L. Dupont, P. Roussel and R. Desfeux, *J. Mater. Chem.*, 2012, **22**, 9806–9812.
12 T. Ukita, Y. Hirose, S. Ohno, K. Hatabayashi, T. Fukumura and T. Hasegawa, *J. Appl. Phys.*, 2012, **111**, 07D909.
13 EU-Directive 2002/95/EC, Restriction of the use of certain hazardous substances in electrical and electronic equipment (RoHS), *Off. J. Eur. Union*, 2003, **46**(L37), 19–23; EU-Directive 2002/96/EC, Waste Electrical and Electronic Equipment (WEEE), *Off. J. Eur. Union*, 2003, **46**(L37), 24–38.
14 S. J. Patwe, V. Katari, N. P. Salke, S. K. Deshpande, R. Rao, M. K. Gupta, R. Mittal, S. Nagabhusan Achary and A. K. Tyagi, *J. Mater. Chem. C*, 2015, **3**, 4570–4584.
15 D. W. Hwang, J. S. Lee, W. Li and S. H. Oh, *J. Phys. Chem. B*, 2003, **107**, 4963–4970.
16 S. Faulkner, S. J. A. Pope and B. P. Burton-Pye, *Appl. Spectrosc. Rev.*, 2005, **40**, 1–31.
17 S. Saitzek, Z. Shao, A. Bayart, P. Roussel and R. Desfeux, *Perovskites and Related Mixed Oxides: Concepts and Applications*, Wiley-VCH, Weinheim, 2015, pp. 233–258.
18 A. Ferri, S. Saitzek, Z. Shao, G. Declercq, J. Costecalde, D. Rémiens, D. Deresmes, D. Troadec and R. Desfeux, *J. Am. Ceram. Soc.*, 2013, **96**(12), 3877–3882.
19 M. Kimura, S. Nanamatsu, T. Kawamura and S. Matsushita, *Jpn. J. Appl. Phys.*, 1974, **13**(9), 1473–1474.
20 Z. Shao, S. Saitzek, P. Roussel, M. Huvé, R. Desfeux, O. Mentré and F. Abraham, *J. Cryst. Growth*, 2009, **311**, 4134–4141.
21 L. Kim, J. Kim, D. Jung, J. Lee and U. V. Waghmare, *Appl. Phys. Lett.*, 2005, **87**, 052903.

22 H. N. Lee, H. M. Christen, M. F. Chisholm, C. M. Rouleau and D. H. Lowndes, *Nature*, 2005, **433**, 395–399.

23 T. Tsurumia, T. Harigai, D. Tanaka, S.-M. Nam, H. Kakemoto, S. Wada and K. Saito, *Appl. Phys. Lett.*, 2004, **85**, 5016.

24 M. Dawber, N. Stucki, C. Lichtensteiger, S. Gariglio and J. M. Triscone, *J. Phys.: Condens. Matter*, 2008, **20**, 264015.

25 W. Tian, J. C. Jiang, X. Q. Pan, J. H. Haeni, Y. L. Li, Q. Chen, D. G. Schlom, J. B. Neaton, K. M. Rabe and Q. X. Jia, *Appl. Phys. Lett.*, 2006, **89**, 092905.

26 T. Shimuta, O. Nakagawara, T. Makino, S. Arai, H. Tabata and T. Kawai, *J. Appl. Phys.*, 2002, **91**, 2290–2294.

27 L. Kim, D. Jung, J. Kim, Y. S. Kim and J. Lee, *Appl. Phys. Lett.*, 2003, **82**, 2118–2120.

28 S. Bose and S. B. Krupanidhi, *Appl. Phys. Lett.*, 2007, **90**, 212902.

29 R. Ranjith, B. Kundys and W. Prellier, *Appl. Phys. Lett.*, 2007, **91**, 222904.

30 R. Ranjith, U. Lüders, W. Prellier, A. Da Costa, I. Dupont and R. Desfeux, *J. Magn. Magn. Mater.*, 2009, **321**, 1710–1713.

31 B. J. Rodriguez, C. Callahan, S. V. Kalinin and R. Proksch, *Nanotechnology*, 2007, **18**, 475504.

32 E. Khestanova, N. Dix, I. Fina, M. Scigaj, J. M. Rebled, C. Magén, S. Estradé, F. Peiró, G. Herranz, J. Fontcuberta and F. Sánchez, *Adv. Funct. Mater.*, 2016, **35**, 6446–6453.

33 D. Martin, J. Müller, T. Schenk, T. M. Arruda, A. Kumar, E. Strelcov, E. Yurchuk, S. Müller, D. Pohl, U. Schröder, S. V. Kalinin and T. Mikolajick, *Adv. Mater.*, 2014, **26**, 8198–8202.

34 C. Aruta, G. Balestrino, R. Desfeux, S. Martellucci, A. Paoletti and G. Petrocelli, *Appl. Phys. Lett.*, 1996, **68**, 926–928.

35 D. Seol, B. Kim and Y. Kim, *Curr. Appl. Phys.*, 2017, **17**, 661–674.

36 R. K. Vasudevan, N. Balke, P. Maksymovych, S. Jesse and S. V. Kalinin, *Appl. Phys. Rev.*, 2017, **4**, 021302.

37 E. Strelcov, Y. Kim, J. C. Yang, Y. H. Chu, P. Yu, X. Lu, S. Jesse and S. V. Kalinin, *Appl. Phys. Lett.*, 2012, **101**, 192902.

38 N. Balke, P. Maksymovych, S. Jesse, A. Herklotz, A. Tselev, C.-B. Eom, I. I. Kravchenko, P. Yu and S. V. Kalinin, *ACS Nano*, 2015, **9**, 6484–6492.

39 C. Li, Y. Cao, Y. Bai, A. Li, S. Zhang and D. Wu, *ACS Appl. Mater. Interfaces*, 2015, **7**, 10146–10151.

40 C. W. Bark, P. Sharma, Y. Wang, S. H. Baek, S. Lee, S. Ryu, C. M. Folkman, T. R. Paudel, A. Kumar, S. V. Kalinin, A. Sokolov, E. Y. Tsymbal, M. S. Rzchowski, A. Gruverman and C. B. Eom, *Nano Lett.*, 2012, **12**, 1765–1771.

41 D. Seol, S. Park, O. V. Varenyk, S. Lee, H. N. Lee, A. N. Morozovska and Y. Kim, *Sci. Rep.*, 2016, **6**, 30579.

42 S. Martin, N. Baboux, D. Albertini and B. Gautier, *Ultramicroscopy*, 2017, **172**, 47–51.

43 A. S. Borowiak, N. Baboux, D. Albertini, B. Vilquin, G. Saint Girons, S. Pelloquin and B. Gautier, *Appl. Phys. Lett.*, 2014, **105**, 012906.

44 Q. N. Chen, Y. Ou, F. Ma and J. Li, *Appl. Phys. Lett.*, 2014, **104**, 242907.

45 Y. Rozier, B. Gautier, G. Hyvert, A. Descamps, C. Plossu, F. Ducroquet and C. Dubourdieu, *Thin Solid Films*, 2009, **517**, 1868–1873.

46 M. Bousquet, J.-R. Duclère, B. Gautier, A. Boulle, A. Wu, S. Députier, D. Fasquelle, F. Rémondière, D. Albertini, C. Champeaux, P. Marchet, M. Guilloux-Viry and P. Vilarinho, *J. Appl. Phys.*, 2012, **111**, 104106.

47 M. Masuduzzaman, S. Xie, J. Chung, D. Varghese, J. Rodriguez, S. Krishnan and M. A. Alam, *Appl. Phys. Lett.*, 2012, **101**, 153511.

48 M.-X. Zhou, B. Chen, H.-B. Sun, J.-G. Wan, Z.-W. Li, J.-M. Liu, F.-Q. Song and G.-H. Wang, *Nanotechnology*, 2013, **24**, 225702.

49 X. Shen, K. Yin, Y. S. Puzyrev, Y. Liu, L. Sun, R.-W. Li and S. T. Pantelides, *Adv. Electron. Mater.*, 2015, **1**, 1500019.

50 J. Son, J. M. LeBeau, S. J. Allen and S. Stemmer, *Appl. Phys. Lett.*, 2010, **97**, 202109.

51 H. P. R. Frederikse, W. R. Thurber and W. R. Hosler, *Phys. Rev.*, 1964, **134**, A442–A445.

52 R. Scherwitzl, P. Zubko, C. Lichtensteiger and J. M. Triscone, *Appl. Phys. Lett.*, 2009, **95**, 222114.

53 S.-R. Eric Yang and S. Das Sarma, *Phys. Rev. B: Condens. Matter Mater. Phys.*, 1988, **37**, 10090–10094.

54 B. Rieder, Semiclassical transport in semiconductor superlattices with boundaries, PhD, Universität Regensburg, 2004.

55 A. Ohtomo and H. Y. Hwang, *Nature*, 2004, **427**, 423–426.

56 G. Herranz, F. Sanchez, N. Dix, M. Scigaj and J. Foncuberta, *Sci. Rep.*, 2012, **2**, 758.

57 F. Lichtenberg, A. Herrnberger, K. Wiedenmann and J. Mannhart, *Prog. Solid State Chem.*, 2001, **29**, 1–70.

58 F. Gunkel, K. Skaja, A. Shkabko, R. Dittman, S. Hoffmann-Eifert and R. Waser, *Appl. Phys. Lett.*, 2013, **102**, 071601.

59 K. Gupta, B. Mandal and P. Mahadevan, *Phys. Rev. B: Condens. Matter Mater. Phys.*, 2014, **90**, 25109.

60 H. W. Jang, D. A. Felker, C. W. Bark, Y. Wang, M. K. Niranjan, C. T. Nelson, Y. Zhang, D. Su, C. M. Folkman, S. H. Baek, S. Lee, K. Janicka, Y. Zhu, X. Q. Pan, D. D. Fong, E. Y. Tsymbal, M. S. Rzchowski and C. B. Eom, *Science*, 2011, **331**, 886–889.

61 S. Hevelia, S. Wang, K. R. Balasubramaniam and P. A. Salvador, *Cryst. Growth Des.*, 2009, **9**, 4546–4554.

62 R. D. Shannon, Central Research and Development Department, *Experimental Station, E.I. Du Pont de Nemours and Company*, Wilmington, Delaware 19898, U.S.A, Published in Acta Crystallographica, 1976, vol. A32, pp. 751–767.

63 L. K. Joseph, K. R. Dayas, S. Damodar, B. Krishnan, K. Krishnankutty, V. P. N. Nampoori and P. Radhakrishnan, *Spectrochim. Acta, Part A*, 2008, **71**(4), 1281–1285.

64 F.-C. Chiu, *Adv. Mater. Sci. Eng.*, 2014, **2014**, 578168.

65 X. Tang, J. Wang, X. Wang and H. Lai-Wah Chan, *Chem. Mater.*, 2004, **16**, 5293–5296.

66 R. Ranjith, W. Prellier, J. W. Cheah, J. Wang and T. Wu, *Appl. Phys. Lett.*, 2008, **92**, 232905.

67 H. Lu, D. Lee, K. Klyukin, L. Tao, B. Wang, H. Lee, J. Lee, T. R. Paudel, L. Q. Chen, E. Y. Tsymbal, V. Alexandrov, C. B. Eom and A. Gruverman, *Nano Lett.*, 2018, **18**, 491–497.